

## **High Power Density PGM-Free Cathodes for Polymer Electrolyte Fuel Cells**

Aman Uddin<sup>a</sup>, Lisa Langhorst<sup>a</sup>, Hanguang Zhang<sup>b</sup>, Leiming Hu<sup>a</sup>, Gang Wu<sup>b</sup>, Shawn Litster<sup>a\*</sup>

<sup>a</sup>, Department of Mechanical Engineering, Carnegie Mellon University, Pittsburgh,  
Pennsylvania 15213, United States

<sup>b</sup>, Department of Chemical and Biological Engineering, University at Buffalo, The State  
University of New York, Buffalo, NY 14260, United States

\*Corresponding authors: [litster@andrew.cmu.edu](mailto:litster@andrew.cmu.edu) (S. Litster)

### **Abstract**

Low cost and high-performing platinum group metal-free (PGM-free) cathodes have the potential to transform the economics of polymer electrolyte fuel cell (PEFC) commercialization. Significant advancements have been made recently in terms of PGM-free catalyst activity and stability.

However, before PGM-free catalysts become viable in PEFCs, several technical challenges must be addressed including cathode's fabrication, ionomer integration, and transport losses. Here we present an integrated optimization of cathode performance that was achieved by simultaneously optimizing the catalyst morphology and electrode structure for high power density. The chemically-doped metal-organic framework (MOF) derived Fe-N-C catalyst we used allows precise tuning of particle size over a wide range, enabling this unique study. Our results demonstrate the careful interplay between the catalyst primary particle size and the polymer electrolyte ionomer integration. The primary particles must be sufficiently large to permit uniform ionomer thin-films throughout the surrounding pores, but not so large as to impact intraparticle transport to the active sites. The content of ionomer must be carefully balanced between sufficient loading for complete catalyst coverage and adequate proton conductivity, while not being excessive and inducing large oxygen transport losses and liquid water flooding. With the optimal 100 nm size catalyst and ionomer loading, we achieved a high power density of 410 mW/cm<sup>2</sup> at rated voltage and a peak power density of 610 mW/cm<sup>2</sup> in an automotive-relevant operating condition.

## **Keywords**

Polymer electrolyte fuel cell, Platinum group metal-free, Metal-organic framework (MOF), Fe-N-C Catalyst, Computed tomography, Ionomer

## **Introduction**

Polymer electrolyte fuel cell (PEFCs) are a key technology for vehicle electrification, particularly in heavy-duty and long-range applications. PEFCs also have significant market potential in portable and stationary power sources. However, high cost and insufficient durability hinder

widespread commercialization of PEFCs. At mass production, the biggest contributor to stack cost (>40%) is the expensive Pt-based catalysts<sup>1</sup> and a recent expert elicitation study showed a strong consensus that the Pt catalyst was the leading barrier to reducing automotive PEFC costs<sup>2</sup>. Given this is a raw material cost, the economies of scale for this component are limited. In addition, global Pt reserves are limited to a small handful of countries outside of the United States, primarily in South Africa. Thus, there remains a long term desire for a low-cost, highly active platinum group metal-free catalyst for PEFCs.

Among all PGM-free catalysts for the acidic oxygen reduction reaction (ORR), iron-nitrogen-carbon (Fe-N-C) catalysts are the most promising<sup>3</sup>. Although some debate remains as to the identity and role of the active sites in these catalysts, the proposed active site is generally attributed to the FeN<sub>4</sub> moiety<sup>4,5,6</sup>. The recently reported performance of these catalysts is approaching that of Pt catalysts<sup>3,5</sup>, with the highest activity being achieved with catalysts derived from MOFs. Several authors reported peak PEFC power density of >900 mW/cm<sup>2</sup> under O<sub>2</sub> and 0.3-0.57 W/cm<sup>2</sup> under air using Fe-N-C based catalysts<sup>4,5,7,8,9</sup>. Despite great progress, the lower volumetric activity (A/m<sup>3</sup>) of PGM-free catalysts versus Pt-based catalysts requires catalyst layers that are one order of magnitude thicker. This thickness combined with the hydrophilic, functionalized carbon surface yields a cathode that is highly sensitive to liquid water flooding and large proton ohmic losses as protons must be conducted across flooded cathodes<sup>10,11</sup>. Additionally, poor proton transport accelerates degradation due to non-uniform reaction current density across the electrode thickness<sup>12</sup>.

Cathode morphology also affects fuel cell performance. Lefevre et al. found that pores (diameter <2 nm) are important in hosting FeN<sub>4</sub> active sites<sup>7</sup>. Wide pore size distributions, including large macropores, provide considerably improved reactant and water transport<sup>9</sup>. Additionally, fuel cell performance is sensitive to ionomer distribution within the thick catalyst layer<sup>10,12</sup>. The ionomer distribution affects ionic conductivity of the electrode<sup>12</sup> and depends on the dispersion of ionomer in solution as well as the surface chemistry and morphology of the electrode<sup>13</sup>. Simply increasing ionomer loading is not beneficial due to increased mass transport losses.

MOF-based catalysts have recently received much attention with a focus on controlling the catalyst morphology to increase active site density and improve fuel cell performance<sup>4,14,15</sup>. In a previous study, the authors from University at Buffalo-SUNY reported the synthesis and ORR activity of chemically-doped Fe-MOF catalysts with variations in particle size without affecting the Fe loading and active site density<sup>15</sup>. The catalyst is prepared by including a Fe precursor in addition to the zinc (Zn) precursor when preparing a zeolitic imidazolate framework (ZIF) particles. Through pyrolysis, the ZIF particles are carbonized, and the Zn is evaporated, leaving behind atomically dispersed Fe coordinated with nitrogen in the carbon matrix. A key advantage of this approach is that the Fe is atomically dispersed without any Fe aggregates. In addition, there is no excessive carbon support additive and the synthesis, being highly streamlined, requires only one heat treatment process without acid leaching or other post-treatments.

Here, we leverage the precise control of the Fe-MOF particle size to perform a systematic study on the assembly of high power density PEFC cathodes with a PGM-free ORR catalyst. Generally, within this field, the development of electrodes is a mostly one-way process, where a catalyst is

synthesized, and the electrode is optimized for that catalyst morphology. In this study, we simultaneously optimize the catalyst morphology and the electrode fabrication to realize high power density. In our study, we prepared cathodes from five different primary particle sizes (40, 60, 80, 100, 150, and 600 nm) using a range of values for the ionomer to carbon mass ratio (I/C). We characterized the cathodes using a variety imaging and electrochemical methods. Through direct visualization of the 3D ionomer distribution and the electrochemical characterization, we broaden our understanding of the structure-performance relationships for PGM-free catalysts in PEFCs.

## **Methods**

### Catalyst synthesis and electrochemical measurement

The details of the Fe-N-C catalyst synthesis were described in our previous publication<sup>14</sup>. In brief, the molar ratio among  $\text{Fe}(\text{NO}_3)_3 \cdot 9\text{H}_2\text{O}$ ,  $\text{Zn}(\text{NO}_3)_2 \cdot 6\text{H}_2\text{O}$ , and 2-methylimidazole was 0.025:1:4.21. The crystal size of the Fe-doped ZIF is controlled by tuning the concentration of metal precursors in the methanol solution. The amount of methanol in the synthesis was adjusted based on its molar ratio to  $\text{Zn}^{2+}$  to prepare Fe-ZIF crystals with various particle sizes. The solvent to precursor ratio was adjusted to precisely tune the particle size from 40 nm to 600 nm. The atomic percentage of iron is consistent between particles of different sizes. In a typical procedure for the 100 nm size catalyst, 3.39 g of zinc nitrate hexahydrate and 100 mg of iron nitrate nonahydrate were dissolved in 300 mL methanol. A 300 mL methanol solution of 3.94 g of 2-methylimidazole was then added into the solution of metal salts. The mixture was kept at 60°C for 24 h. Then the precipitant was collected by centrifuging and washing with ethanol for three times. The obtained solid was dried

at 60°C for eight hours under vacuum to obtain the precursor. The catalyst was obtained by heating the dried precursor at 1100 °C in a tube furnace for 1 h under N<sub>2</sub> flow.

All rotating disk electrode (RDE) measurements were carried out using an electrochemical workstation (CHI760b) coupled with a rotating-ring disc electrode (RRDE, Pine, AFMSRCE 3005) in a three-electrode cell at room temperature. A graphite rod and a Hg/HgSO<sub>4</sub> (K<sub>2</sub>SO<sub>4</sub>-sat., 0.70 V vs. RHE) electrode were employed as the counter and reference electrodes, respectively. An RRDE with a disk diameter of 5.6 mm covered by a thin film of the catalyst was used as the working electrode. To prepare the working electrode, each catalyst was mixed with isopropanol and a 5wt% Nafion solution to produce an ink that was drop-cast onto the RDE and air-dried at 60°C. The loading of the catalyst was controlled at 0.8 mg/cm<sup>2</sup> in this work for all measurements. To determine the electrocatalytic activity for the ORR, steady-state polarization curves were recorded in O<sub>2</sub>-saturated 0.5 M H<sub>2</sub>SO<sub>4</sub> using discrete potential steps of 0.05 V at intervals of 30 s from 1.0 V to 0 V vs. RHE at a rotation rate of 900 rpm.

#### Ink and MEA preparation

The catalyst/ionomer slurry was prepared with a solvent to ionomer mass ratio of 60. First, a solvent mixture was prepared with equal parts isopropanol and deionized water (18.2 mΩ·cm). The solvent mixture was sonicated for five minutes. Once sonicated, the solvent was added to the catalyst drop-by-drop. The mixture was then sonicated for ten minutes. The required amount of 5 wt% Nafion<sup>®</sup> solution was then added to the mixture drop-by-drop. The mixture was sonicated for three hours in a bath sonicator, and the temperature of the bath was maintained below 30°C.

The catalyst ink was coated onto SGL 25BC gas diffusion layer (GDL) using a manual doctor blade technique: First, a GDL (2.4×2.4 cm) was placed on top of a hot plate set to 60°C. Then 25  $\mu\text{l}$  of ink was coated on the GDL and dried and then coated again until the catalyst loading of  $\sim 4.0 \text{ mg cm}^{-2}$  was reached. A  $5 \text{ cm}^2$  area of the catalyst coated GDL was used as the cathode in the MEA. A commercial Pt-catalyzed GDE ( $0.3 \text{ mgPt cm}^{-2}$ , Fuelcelletc, College Station, TX) was used for the anode. The cathode and the anode were hot-pressed (500 psi) onto a membrane at 130°C for 4 minutes. Unless otherwise stated, all the membranes were Nafion<sup>®</sup> 212. The MEAs was assembled into  $5 \text{ cm}^2$  commercial fuel cell hardware (Scribner Associates Inc., Southern Pines, NC).

### Fuel cell testing

Fuel cells were tested using a commercial test station (850e, Scribner Associates Inc., Southern Pines, NC). First, the cell was heated to 80°C with 200 sccm of  $\text{N}_2$  in the anode and cathode for two hours to hydrate the membrane and ionomer. Then, cyclic voltammetry (CV) was conducted using a Potentiostat (SP-150, BioLogic, Seyssinet-Pariset, France) with a Booster (VMP3B-20, BioLogic, Seyssinet-Pariset, France) at a scan rate of 20 mV/sec over the range of 0.04 – 1 V. During CV, 200 sccm of  $\text{H}_2$  and  $\text{N}_2$  were fed through anode and cathode, respectively at 100% RH and the cell temperature was maintained at 80°C. After CV, electrochemical impedance spectroscopy (EIS) was performed at 0.5 V in the same operating conditions as the CV measurement with a voltage perturbation of 10 mV and a frequency range from 100,000 to 0.01 Hz. Then, polarization curves were measured with 200 sccm of  $\text{H}_2$  and air or  $\text{O}_2$  in anode and

cathode at 100% RH, respectively. The cell and humidifier temperatures were kept at 80°C. 1.0 atm partial pressure of H<sub>2</sub> and air/O<sub>2</sub> was maintained by setting 50 kPa gauge pressure in the anode and cathode. Lastly, polarization curves were measured at 60% RH and 1 atm partial pressure of H<sub>2</sub> and air or O<sub>2</sub> was maintained by setting 30 kPa gauge pressure in the anode and cathode.

### Nano-CT sample preparation and imaging

All cathode GDEs were analyzed using nano-CT (UltraXRM L200, Xradia, Inc., Pleasanton, CA) with an 8 keV rotating copper anode X-ray source. Details of this process can be found from previous publication<sup>9</sup>. In brief, a small portion of the GDE, 0.5 mm × 0.5 mm, was mounted to a flattened pin head using epoxy adhesive. The catalyst layer on the specimen was further trimmed down with a low energy laser beam (355 nm wavelength ultraviolet laser) using a high resolution (~1 μm) laser mill (ESI, QuikLaze 50ST2, Portland, OR). The laser ablation resulted a pillar shaped catalyst layer segment with a cross-sectional area of 40×40 μm so that it would remain within the field of view (FOV) of the nano-CT. The catalyst pillar was then ion-exchanged with saturated cesium-sulfate (Cs<sub>2</sub>SO<sub>4</sub>, Sigma-Aldrich, St. Louis, MO) solution in order to increase the X-ray attenuation of the Nafion<sup>®</sup> ionomer during the imaging process.

The catalyst pillar was imaged in 3D using the nano-CT's large field of view (LFOV) absorption contrast mode. The LFOV optics provide a voxel size of 64 nm, a spatial resolution of 120 -150 nm, and a 65 μm FOV. The absorption contrast mode provides X-ray contrast based on material density and atomic number. For the samples imaged, the absorption mode identifies the spatial

distribution of the cesium stained Nafion® ionomer. The reconstructed image from the nano-CT characterization was then analyzed using commercial software (Avizo Fire, FEI, Hillsboro, OR).

The cathode and MEA structures were additionally imaged by plasma focused ion beam – scanning electron microscopy (pFIB-SEM) and micro-CT, respectively. The pFIB-SEM (Helios DualBeam, FEI, Hillsboro, OR) imaging was performed using with 2 nm pixels and 4 nm slice thicknesses. The micro-CT ( $\mu$ CT 50, Scanco Medical, Switzerland) imaging was performed on section of MEA including the anode and cathode GDLs.

## **Results and Discussion**

### Rotating Disk Electrode Characterization of Catalysts

Before preparing PEFC cathodes, it is important to verify the activity ex-situ under well-defined RDE conditions. The Fe-MOF catalyst used here shows very high ORR activity in RDE studies. **Figures 1a,b** show SEM images of nominally 40 nm and 100 nm catalyst particles. As they show, the catalyst's half-wave potential in RDE IV-curve measurements is typically  $\sim 0.87$  V with an  $0.8 \text{ mg/cm}^2$  loading in 0.5 M sulfuric acid. Our preferred catalyst activity metric for electrode development is the mass activity, since it normalizes the RDE loading and better reflects how the catalyst will work in a PEFC cathode given the mass activity's relation to required electrode thickness<sup>16</sup>. The 0.9 V mass activity for these catalysts is typically around 1 A/g. In prior work<sup>15</sup>, RDE testing showed a significant apparent activity dependence on particle size (see **Fig. S1**). But, when the I/C ratio of the RDE is optimized for a given particle size, there is little difference in the activity between the different particle size. **Figs. 1c,d** shows the RDE polarization curves for 40

nm and 150 nm catalyst particles with varying I/C ratios. The optimal ionomer loading for 40 nm was an I/C of 0.1, while it was 0.4 for the 150 nm catalyst. At these optimal I/C values, both catalysts present a 0.9 V mass activity of 1.0 A/g, based on the mass of the MOF-derived catalyst. Considering their equal atomic iron to carbon ratio of 2.5%, we can state that within this range of particle sizes (<200 nm), the efficacy of the active sites is independent of the particle size. The origin of the ionomer loading dependence is the subject of future work. The large degree of limiting current variation in **Fig. 1c** is attributed to surface roughness when preparing RDEs with high loadings of large catalyst aggregates, which are more pronounced for the smaller 40 nm primary particles.

### Cathode Morphology

Gas diffusion electrodes (GDEs) for PEFC testing were prepared from the catalyst by mixing with ionomer and additional solvents to prepare a slurry that we manually doctor bladed onto commercial gas diffusion layers (GDLs). We prepare GDEs instead of catalyst coated membranes (CCMs) because GDEs reduced flooding in preliminary tests. We ascribed the reduced flooding to the elimination of interfacial voids between the catalyst layer and MPL with GDEs as observed by our micro-scale X-ray computed tomography (micro-CT) imaging, which shows the conformal interface between the two layers. A similar conclusion was also recently reported by Liu et al.<sup>17</sup> **Figures 2 a-d and Fig. S2** show the SEM images of GDEs prepared with primary particles of varying size. The SEM images show that the catalyst with smaller particles formed a more continuous structure during synthesis and also formed mostly large and dense aggregates (up to 20-30  $\mu\text{m}$  in diameter). Catalysts with larger primary particles form fewer large aggregates and the

primary particles are well-separated and distinct (**Figs. 2 c,d and Fig. S2b**). As **Fig. 2a** shows, with the 40 nm catalyst, the majority of the catalyst is found in large aggregates, forming large secondary pores visible in the SEM images. In contrast, with 100 nm and 600 nm catalyst, the majority of the catalyst was found in small aggregates (relative to the primary particle size) that agglomerated to form a continuous layer with negligible large secondary pores.

Ideally, the ionomer forms continuous films over the surface of the primary particles without excessive thickness to inhibit mass transport. To evaluate the ionomer distribution in the cathode, we used nano-CT imaging of ionomer that is achieved by staining the ionomer through ion exchange with cesium as reported by Komini Babu et al.<sup>10</sup>, where the Cs ions provide adequate atomic number X-ray absorption contrast versus the carbon catalyst. It should be noted that this ion staining method has been previously used for imaging ionomer using transmission electron microscopy (TEM)<sup>18,19</sup>. **Figure 3 and Fig. S3** show the nano-CT images that we normalized by internal reference intensities for directly comparing the local density of Cs-stained ionomer between samples. Brighter regions in the image indicate a high concentration of the acidic groups in the ionomer and the brightest regions reflect the concentration of the bulk polymer electrolyte. **Supplemental Movie 1** shows 3D renderings of the ionomer distributions. In the 40 nm size catalyst (**Fig. 3a**), the interior of the large catalyst aggregates (>5  $\mu\text{m}$ ) is mostly free of ionomer, and the majority of the ionomer is found in thick films around the aggregates that likely incorporate the small fraction of small aggregates. Ionomer did not infiltrate into the fused aggregates in spite of using high ionomer content (I/C 1) compared to the all the other catalysts (I/C 0.6) shown in **Fig. 3**. As **Figs. 3c,d** show, the 100 nm and 600 nm size catalysts feature good ionomer infiltration

and uniform primary particle coverage. The 60 nm catalyst shown in **Fig. 3b** presents an intermediate case, where a greater fraction of ionomer infiltrates the aggregates, but there are still dense layers of ionomer around the large aggregates. Consistent with the reduced primary particle surface area, the thick film covering the 600 nm primary particles is seen in **Fig. 3d**. The thickness of the ionomer film was calculated using a geometric ionomer thickness model that is described in the Supplemental Information. **Table S1** lists the estimated thicknesses, including estimates of 7 nm for 100 nm catalyst and 40 nm for the 600 nm catalyst, each with an I/C value of 0.6.

The thin-film ionomer coating of the 100 nm particles with an I/C of 0.6 was confirmed by high resolution SEM imaging of a cross-section prepared by plasma focused ion beam (PFIB) milling. **Figure 4** shows the 4  $\mu\text{m}$  x 4  $\mu\text{m}$  cross-section where uniform particle size with commensurate uniform pore size. **Supplemental Movie 2** shows the successive removal of 4 nm slices across the depth of the electrode, evidencing the consistent size of the ionomer-coated particles without any obvious regions of agglomerated ionomer. Combining the nano-CT imaging result of uniform ionomer distribution at the aggregate-scale and the pFIB-SEM showing a solid structure morphology consistent with the primary particle aggregates, the conclusion must be drawn that the significant ionomer volume is present as a thin-film around the primary particles.

#### Optimizing Primary Particle Size for PEFC Performance

Performance within a PEFC is a key viability test for PGM-free catalysts since it requires the catalyst to facilitate the gas and proton transport through the cathode thickness and within the local microstructure to the active site, which are properties not revealed in RDE testing. The GDEs

described above were combined with a commercial membrane and commercial anode GDE and tested in standard fuel cell hardware under a wide range of operating conditions with a variety of electrochemical diagnostics. **Figure 4** shows the cross-section of the pressed MEAs, including the gas diffusion layers (GDLs) as image by micro-CT; **Supplemental Movie 3** shows cross-sectional imaging of the MEA's internal morphology. The micro-CT shows how hot pressing of the GDEs onto the membrane formed uniform contact between the membrane and the rough surfaces of the GDEs seen in **Fig. 2**.

**Figures 5 a,b** shows the polarization curves obtained with both fully-humidified air and pure O<sub>2</sub> oxidant gases using catalysts with different primary particles and an I/C of 0.6. The 60 nm catalyst yielded the highest currents in both the high voltage activity and low voltage mass transport limited regions of the polarization curve. The maximum power densities of this catalyst were 385 and 850 mW/cm<sup>2</sup> in air and O<sub>2</sub>, respectively and the power density in air at a fuel cell voltage of 0.7 V was 228 mW/cm<sup>2</sup> (**Fig. S4**). The PEFC performance with 80 nm and 100 nm size catalysts was close to the 60 nm size catalyst. The MEA with 600 nm size catalyst had the lowest current densities in the activation and mass transport-limited regions of the polarization curve. The second largest 150 nm size catalysts also showed similar low performance. Despite performing well in RDE testing (**Fig. S1**), the 40 nm catalyst showed poor performance in PEFC testing, where its apparent activity was below that of the 60-100 nm catalysts and was highly transport limited at lower voltages.

To evaluate the severity of flooding, we measured additional polarization curves at a lower relative humidity (RH) of 60%. **Figure 5c** shows the polarization curves obtained with air for the 40 nm

and 100 nm size catalysts at 60% RH and 100% RH. Current densities are lower at high voltage at 60% RH because of Ohmic losses, whereas differences at low voltage indicated the change in mass transport resistances due to flooding. The total gas pressures were adjusted to maintain the same oxygen partial pressures, *i.e.* 1.0 atm. Cell performance is improved at 60% RH compared to 100% RH in the mass transport region for both catalysts due to reduced liquid water accumulation. The 40 nm size catalyst's current density increases 30% at 0.4 V with 60% RH vs. 100%, whereas the increase is only 10% for the 100 nm size catalyst. The high degree of flooding with the highly aggregated 40 nm primary particles is likely a result of the thick ionomer films increasing hydrophilicity and the degree of flooding rather than an effect of the smaller pores between the primary particles in the aggregates. The increased wettability with increased ionomer coverage and thicker films over carbon particles was previously shown by Li et al.<sup>20</sup> The low voltage current densities of all other sized catalyst also increased at 60% RH versus 100% (**Fig. S5**).

With the goal of improving fuel cell performance by optimizing ionomer loading, best performing 60 nm, 80 nm, and 100 nm size catalysts were used to prepare MEAs with a range of ionomer loading. **Figure 5d** shows the performance curves obtained under air for the 80 nm size catalyst and **Fig. S6** shows the performance for the 60 nm and 100 nm size catalysts with various I/C ratios. In the case of the 60 nm and 100 nm size catalysts, higher ionomer loading (I/C of 0.8) resulted in higher activity, but also higher mass transport resistances relative to the MEA with an I/C of 0.6 (**Figs. S6a,b,e,f**). In the case of the 80 nm size catalyst, the overall best fuel cell performance was achieved with an I/C of 0.8 (**Fig. 5d**). The maximum power densities of this catalyst with an I/C 0.8 were 390 and 870 mW/cm<sup>2</sup> in air and O<sub>2</sub>, respectively, and the power density with air at a fuel

cell voltage of 0.7 V was 254 mW/cm<sup>2</sup>. The cell performance of the 80 nm size catalyst with an I/C of 1 was much lower than with an I/C of 0.6 or 0.8, likely due to liquid water flooding.

As the polarization curve results above show a significant sensitivity to ionomer loading at the lower levels of I/C, we performed electrochemical analyses of the ionomer coverage as a function of I/C. More specifically, we performed N<sub>2</sub>/H<sub>2</sub> cyclic voltammetry (CV) measurements for the MEAs over a wide range of RH levels and then evaluated the change in the capacitive surface area from the voltammograms. Our approach was inspired by the work of Padgett et al.<sup>21</sup> and Shinozaki et al.<sup>22</sup> where they measured the electrochemical surface area of Pt/C catalysts at various RH to evaluate the amount of Pt in contact with ionomer since at low RH values the internal ionomer-free catalyst pores are dry and no longer provide a water-based proton transport pathway. **Figure 6 a,b** shows CVs of an MEA prepared from the 80 nm size catalyst with an I/C of 0.6 and the corresponding variation in integrated area enclosed by the CV with RH for cells with various I/C values. In **Figure 6b**, the integrated CV area for a given cell was normalized by that area at 100% RH. Here we consider the integrated area of the CV as proxy for the wetted surface area of the catalyst. Above 50% RH, the surface area is fairly insensitive to RH, whereas the surface area is dramatically reduced below 40% RH. The large loss of surface area at low RH indicates that a significant fraction of the capacitive catalyst area at high RH is not in contact with Nafion ionomer. Based on the observed drop in surface area occurring at roughly 40% RH, we can infer that majority of the surface area probed at higher RH is present in sub-5 nm pores through evaluating the Kelvin equation for capillary condensation. In other words, ionomer did not infiltrate the small pores. Since the smallest Nafion ionomer micelle size is 1–5 nm,<sup>23</sup> ionomer penetration into pores less

than 2 nm is challenging<sup>22,24</sup>, and we suspect little, if no, ionomer infiltrates the primary particle and the ionomer chiefly coats the outer surface of the primary particles. Based on the simple geometry of the primary particles, we can also assert that only a small fraction of the surface area seen in the CVs is due to the outer surface of the particles. Therefore, proton transport happens through water in the microporous primary particles. At high RH, the increase of ionomer content from I/C 0.6 to 0.8 caused a minor increase in surface area indicating slightly better coverage of the primary particles or minor amounts of ionomer infiltration into the primary particles, but there was no significant change in surface area for increasing I/C to 1. This indicates that the extra ionomer likely only increased the thickness of the ionomer film, decreased porosity, increased transport resistance, and caused flooding as shown in **Fig. 5d**. The surface area of the 60 nm and 100 nm size catalysts also show similar sensitivity to RH (see **Fig. S7**).

To understand the impact of particle size and I/C on electrode ohmic losses, we measured the electrochemical impedance spectroscopy (EIS) response of the cells with various particle size catalysts and I/C ratios (**Fig. 6c**). There was no significant difference in HFR from cell to cell and HFR is subtracted from our Nyquist plot comparisons. These data sets were then analyzed based on the blocking electrode transmission line model.<sup>25</sup> The proton conduction resistance of the electrode can be approximated from the horizontal dimension of the  $\sim 45^\circ$  line originating at the HFR. In other words, the real impedance at the point where the spectra turns vertical in **Fig. 6c** can be considered as 1/3 the electrode resistance since we have subtracted the HFR. We observe that the larger particles (150 and 600 nm) presented notably higher resistances, whereas the 40 nm and 100 nm size catalysts spectras almost perfectly overlap with the lowest resistance. The estimated

effective proton conductivity with 100 nm catalyst is approximately 2 S/m, whereas that value for the 600 nm catalyst is approximately 0.6 S/m. We attribute these conductivity findings to a combination of factors. First, the microporous carbon has intrinsic proton conductivity through the water domains that provides a path between branches of ionomer. Second, larger particles yield greater distances between ionomer, increasing the inner particle water domain resistance. The variation in the resistances for the 40-100 nm catalysts could be due to systematic variation in primary particle size, aggregate size, and connectivity as well as more stochastic sources of variability. For example, the highly agglomerated ionomer in the 40 nm particle catalyst case has low tortuosity and provides good conductivity through bulk-like ionomer. Similar results were found by Komini Babu et al.<sup>10</sup> by performing transport simulations on 3D images of ionomer distributions in PGM-free cathodes. However, the variability in the apparent resistance in the 40-100 nm size is relatively small compared to the difference to 150 nm and 600 nm.

#### High MEA Power Density and Activity

Although the 60 and 80 nm size catalysts show improved ionomer infiltration and good fuel cell performance, they still form larger solid fused aggregates that are difficult to break up by milling. Images of the aggregates are shown in **Fig. 3b** and **Fig. S3**. Unfortunately, the variability in the size and number of large aggregates with these particles led to the results that are not sufficiently repeatable from catalyst batch to batch (**Fig. S8**). However, using the slightly larger 100 nm size catalyst, we have seen uniform ionomer distribution, fewer large aggregates (**Figs. 2c, 3c**), and repeatable MEA performance across MEA fabrication and catalyst batches (**Fig. S9**). Using this

100 nm catalyst with 1 atm dry air partial pressure at 80°C, the best current density achieved at 0.8 V was 113 mA/cm<sup>2</sup> and the highest power density achieved at 0.7 V was 268 mW/cm<sup>2</sup> (383 mA/cm<sup>2</sup>) (**Fig. S9**). To the best of our knowledge, this is the highest reported current density at 0.8 V in these operating conditions for PGM-free PEFCs. Wan et al.<sup>26</sup> and Myers et al.<sup>27</sup> recently achieved a similarly high value of 0.8 V current of 105 mA/cm<sup>2</sup>.

To demonstrate higher fuel cell performance, we tested a cell using the 100 nm size catalyst and a Nafion 211 membrane at an automotive-relevant operating condition of 94°C with 1.7 atm dry air partial pressure. The thinner Nafion 211 membrane was used to reduce ohmic resistance and increase the rate of water removal to the anode. The higher cell temperature increased mass transfer rates and ORR kinetics and also reduced the rated voltage to meet the heat rejection constraint set by US Department of Energy ( $Q/\Delta T < 1.45$  kW/°C, where Q is the stack heat load for an 80-kWe net power PEFC system and  $\Delta T$  is the difference between the stack coolant temperature and 40°C ambient temperature)<sup>28</sup>. Thus, at 94°C, the rated voltage is 0.67 V. A relatively high cathode flow rate (1000 sccm) was used to run the cell with minimal oxygen depletion along the channel length. With this cell assembly and operating point, we have achieved a current density of 150 mA/cm<sup>2</sup> at 0.8 V, a power density of 347 mW/cm<sup>2</sup> at 0.7 V, and a rated voltage power density of 410 mW/cm<sup>2</sup> at 0.67 V (see **Fig. 7a**). With 80% RH feed gases, we also achieved the peak power densities of 610 mW/cm<sup>2</sup> in air and 1.14 W/cm<sup>2</sup> in O<sub>2</sub> (**Fig. 7a**).

An additional set of fuel cell measurements were conducted to evaluate the cathode activity following the common practice of benchmarking by the current density at 0.9 V<sub>HFR-free</sub> at 80°C with

1 atm O<sub>2</sub> at 100% RH. The best MEA performance at 0.9 V<sub>HFR-free</sub> achieved was 28.5 mA/cm<sup>2</sup> under 1 atm O<sub>2</sub> at 80°C (**Fig. 7b**). This is close to the U.S. DoE 2025 technical target for PGM-free catalyst based MEA activity of 44 mA/cm<sup>2</sup> at 0.9 V<sub>HFR-free</sub>. In this case, a current density of 44 mA/cm<sup>2</sup> was achieved at 0.89 V<sub>HFR-free</sub>. For this result, we used the 100 nm size catalyst with a loading of 6 mg/cm<sup>2</sup>, an I/C of 1, and a thick Nafion 117 membrane. Recently, Zelenay et al.<sup>29</sup> reported current densities ranging from 29-36 mA/cm<sup>2</sup> at 0.9 V<sub>HFR-free</sub> with CM-PANI-Fe-C(Zn) catalyst with a higher loading of 6.8 mg/cm<sup>2</sup>, yielding a similar MEA mass activity to that reported here.

### Stability of Fe-MOF Catalyst

Despite the significant advances in activity, PGM-free catalysts still lack the sufficient stability for most commercial applications, especially transportation. Here, we evaluated the stability of the best performing 100 nm size catalyst and the MEA durability by a potentiostatic hold at 0.7 V in a H<sub>2</sub>/air fuel cell. **Figure 8a** presents current density time series measured during the potential hold at 0.7 V and **Fig. 8b** shows the polarization curves measured intermittently during the test. Current densities at 0.7 V from all polarization curves are shown in **Fig. 8a** using cross markers in the plot. Stability results demonstrate two distinct degradation mechanisms: a short time-scale loss that occurs over the first 12 hours, and a constant decay rate. We also find a minor recovery in performance after each intermittent polarization curve followed a short time-scale decay back to the prior slow linear decay. The slow, linear decay rate after 12 hours is 1 mA/cm<sup>2</sup>/h. The behavior observed in MEAs is in good agreement with the measurement in 0.5 M H<sub>2</sub>SO<sub>4</sub> electrolytes during the ORR<sup>30</sup>, suggesting that the degradation is likely due to an activity loss of the PGM-free catalyst.

Efforts are underway to understand the origins of the two separate degradation mechanisms and the reversibility of the short-time scale degradation. Proposed degradation mechanisms include carbon corrosion, demetallation, protonation, radical attack, and micropore flooding<sup>31</sup>.

## **Summary**

Here we have presented the systematic integration of a PGM-free ORR catalyst with ionomer to prepare high power density cathodes for PEFCs. The key aspect of this work was elucidating the correlation between the catalyst's particle size and quality of ionomer integration for optimized proton conduction and oxygen transport. This novel study leverages our recent achievement of PGM-free catalyst synthesis in accurately controlling primary particle sizes without significant variation in the catalyst's iron content or volumetric activity. The best performance was achieved by identifying the optimal ionomer loading with the catalyst having favorable particle and aggregate sizes. If the catalyst primary particles are too small (e.g., < 80 nm), the meso- and macropores between the primary particles are too narrow for adequate ionomer infiltration into the aggregates during ink processing. Furthermore, with this family of catalysts, small primary particles led to larger-sized aggregates that exacerbated this issue. In contrast, when the primary particles are too large the electrodes feature a proton conduction resistance due to the tortuous ionomer paths around the large particles that also have a higher internal resistance for proton conduction through the water domains in the catalyst micropores. In addition, the lower surface area of larger particles entails thicker ionomer films for the same volume fraction of ionomer. A sufficiently high volume fraction is needed for proton conduction, but thick ionomer films become more hydrophilic causing flooding, swell with water, and block gas pores yielding large mass

transport voltage losses. In this study, the most repeatable and uniform ionomer distribution and fuel cell performance was achieved using the catalyst with 100 nm primary particles. Based on these understandings of particles sizes and ionomer content, a high power density of 410 mW/cm<sup>2</sup> was achieved at the rated voltage 0.67 V. We also achieved the peak power density of 610 mW/cm<sup>2</sup> in air and 1.14 W/cm<sup>2</sup> in O<sub>2</sub>. This is roughly a third of the performance from the state of the art with Pt-alloy catalysts, which is very promising for the future use of PGM-free cathodes in commercial PEFCs. However, the degradation rate of PGM-free cathodes, especially the 1 mA/cm<sup>2</sup>/h rate at a typical operating voltage of 0.7 V, still requires significant improvement for PGM-free cathodes to be a viable alternative to their PGM counterparts.

## **ASSOCIATED CONTENT**

Supporting Information:

SEM images of catalyst and GDE; cyclic voltammetry and polarization curves obtained for MEAs prepared from varied particle sizes and varied I/C; repeatability of polarization curves; details of ionomer ionomer thickness model

## **AUTHOR INFORMATION**

Corresponding Author

\*E-mail:litster@andrew.cmu.edu.

### **Authors contributions**

A. U. contributed to the project planning, experimental work, characterization, data analysis and writing of the manuscript. L. L. contributed to the experimental work, characterization, data

analysis and writing of the manuscript. H. Z. contributed to the catalyst synthesis, characterization, and data analysis. L. H. contributed to the characterization and data analysis. G. W. contributed to the catalyst synthesis, data analysis, and review of the manuscript. S. L. contributed to the project planning, data analysis and writing of the manuscript.

### **Acknowledgement**

This material is based upon work supported by the U.S. Department of Energy's Office of Energy Efficiency and Renewable Energy (EERE) under the Fuel Cell Technologies Office (FCTO) under Award Number DE-EE0008076. The authors gratefully acknowledge research support from the Electrocatalysis Consortium (ElectroCat), established as part of the Energy Materials Network under the U.S. Department of Energy, Office of Energy Efficiency and Renewable Energy, Fuel Cell Technologies Office, under Contract Number DE-EE0008076.

### **Disclaimer**

This report was prepared as an account of work sponsored by an agency of the United States Government. Neither the United States Government nor any agency thereof, nor any of their employees, makes any warranty, express or implied, or assumes any legal liability or responsibility for the accuracy, completeness, or usefulness of any information, apparatus, product, or process disclosed, or represents that its use would not infringe privately owned rights. Reference herein to any specific commercial product, process, or service by trade name, trademark, manufacturer, or otherwise does not necessarily constitute or imply its endorsement, recommendation, or favoring by the United States Government or any agency thereof. The views and opinions of authors

expressed herein do not necessarily state or reflect those of the United States Government or any agency thereof.

## References

1. Papageorgopoulos, D., Fuel Cell R&D Overview, *Annual Merit Review and Peer Evaluation Meeting*, US Dept. of Energy, Washington, D.C., April 29, 2019.
2. Whiston, M., Azevedo, I. L., Litster, S., Whitefoot, K. S., Samaras, C., & Whitacre, J. F. Expert assessment of the cost and expected future performance of proton exchange membrane fuel cells for vehicles. *Proceedings of the National Academy of Sciences* **116**, 4899-4904 (2019).
3. Wu, G. & Zelenay, P. Nanostructured nonprecious metal catalysts for oxygen reduction reaction. *Acc. Chem. Res.* **46**, 1878–1889 (2013).
4. Proietti, E. Jaouen, F., Lefèvre, M., Larouche, N., Tian, J., Herranz, J., & Dodelet, J. Iron-based cathode catalyst with enhanced power density in polymer electrolyte membrane fuel cells. *Nat. Commun.* **2**, 416 (2011).
5. Chung, H. T., Cullen, D. A., Higgins, D., Sneed, B. T., Holby, E. F., More, K. L. & Zelenay, P. Direct atomic-level insight into the active sites of a high-performance PGMfree ORR catalyst. *Science*. **357**, 479–484 (2017).
6. Wu, G., More, K. L., Johnston, C. M. & Zelenay, P. High-performance electrocatalysts for oxygen reduction derived from polyaniline, iron, and cobalt. *Science* **332**, 443–447 (2011).

7. Lefèvre, M., Proietti, E., Jaouen, F. & Dodelet, J. P. Iron-Based catalysts with improved oxygen reduction activity in polymer electrolyte fuel cells. *Science* **324**, 71–74 (2009).
8. Shui, J., Chen, C., Grabstanowicz, L., Zhao, D. & Liu, D.-J. Highly efficient nonprecious metal catalyst prepared with metal–organic framework in a continuous carbon nanofibrous network. *Proc. Natl. Acad. Sci.* **112**, 10629–10634 (2015).
9. Banham, D., Kishimoto, T., Zhou, Y., Sato, T., Bai, K., Ozaki, J., Imashiro, Y. & Ye, S. Critical advancements in achieving high power and stable nonprecious metal catalyst – based MEAs for real-world proton exchange membrane fuel cell applications. *Science Advances* **4**, 1–7 (2018).
10. Komini Babu, S., Chung, H. T., Zelenay, P. & Litster, S. Resolving Electrode Morphology’s Impact on Platinum Group Metal-Free Cathode Performance Using NanoCT of 3D Hierarchical Pore and Ionomer Distribution. *ACS Appl. Mater. Interfaces* **8**, 32764–32777 (2016).
11. Babu, S. K., Chung, H. T., Zelenay, P. & Litster, S. Modeling Electrochemical Performance of the Hierarchical Morphology of Precious Group Metal-Free Cathode for Polymer Electrolyte Fuel Cell. *J. Electrochem. Soc.* **164**, F1037–F1049 (2017).
12. Banham, D., Kishimoto, T., Sato, T., Kobayashi, Y., Narizuk, K., Ozaki, J., Zhou, Y., Marquez, E., Bai, K. & Ye, S. New insights into non-precious metal catalyst layer designs for proton exchange membrane fuel cells: Improving performance and stability. *J. Power Sources* **344**, 39–45 (2017).
13. Artyushkova, K., Workman, M. J., Matanovic, I., Dzara, M. J., Ngo, C., Pylypenko, S., Serov, A. & Atanassov, P. Role of Surface Chemistry on Catalyst/Ionomer Interactions for

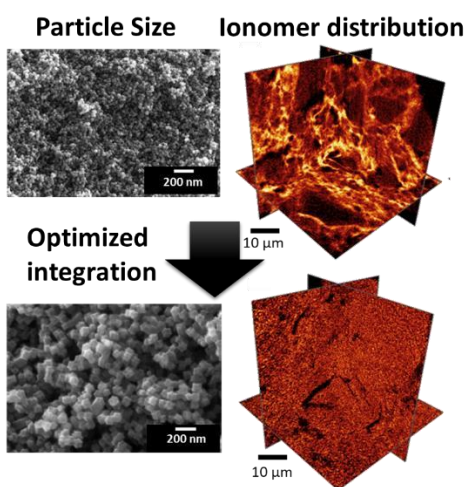
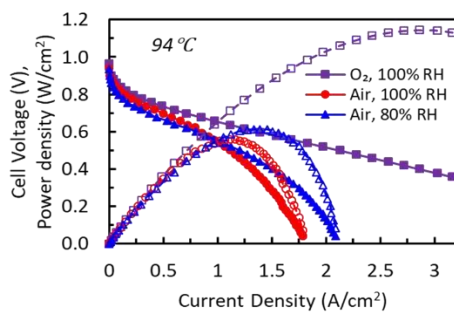
- Transition Metal-Nitrogen-Carbon Electrocatalysts. *ACS Appl. Energy Mater.* **1**, 68-77 (2018).
14. Armel, V., Hannauer, J. & Jaouen, F. Effect of ZIF-8 Crystal Size on the O<sub>2</sub> ElectroReduction Performance of Pyrolyzed Fe–N–C Catalysts. *Catalysts* **5**, 1333–1351 (2015).
  15. Zhang, H., Hwang, S., Wang, M., Feng, Z., Karakalos, S., Luo, L., Qiao, Z., Xie, X., Wang, C., Su, D., Shao, Y. & Wu, Gang. Single Atomic Iron Catalysts for Oxygen Reduction in Acidic Media: Particle Size Control and Thermal Activation. *J. Am. Chem. Soc.* **139**, 14143–14149 (2017).
  16. Beltrán, D.E. & Litster, S. Half-Wave Potential or Mass Activity? Characterizing Platinum Group Metal-Free Fuel Cell Catalysts by Rotating Disk Electrodes. *ACS Energy Letters* **4**, 1158-1161 (2019).
  17. Liu J., Talarposhti, M. R., Asset, T., Sabarirajan, D. C., Parkinson, D. Y., Atanassov, P. & Zenyuk, I. V. Understanding the Role of Interfaces for Water Management in Platinum Group Metal-Free Electrodes in Polymer Electrolyte Fuel Cells. *ACS Appl. Energy Mater.* **2**, 3542–3553 (2019).
  18. Rieberer, S., Norian, K. H. Analytical Electron Microscopy of Nafion Ion Exchange Membranes. *Ultramicroscopy* **41** (1–3), 225–233 (1992).
  19. Fujimura, M., Hashimoto, T., Kawai, H. Small-Angle X-Ray Scattering Study of Perfluorinated Ionomer Membranes. 2. Models for the Ionic Scattering Maximum. *Macromolecules* **15** (1), 136– 144 (1982).
  20. Li X., Feng X., Zhang K., Ye S., Kwok D. Y., Birss, V. Wettability of Nafion and Nafion/Vulcan Carbon Composite Films. *Langmuir* **28** (16), 6698-6705 (2012).

21. Padgett, E., Andrejevic, N., Liu, Z., Kongkanand, A., Gu, W., Moriyama, K., Jiang, Y., Kumaraguru, S., Moylan, T. E., Kukreja, R. & Muller, D. A. Connecting Fuel Cell Catalyst Nanostructure and Accessibility Using Quantitative Cryo-STEM Tomography. *J. Electrochem. Soc.* **165**, F173-F180 (2018).
22. Shinozaki, K., Yamada, H. & Morimoto, Y. Relative Humidity Dependence of Pt Utilization in Polymer Electrolyte Fuel Cell Electrodes : Effects of Electrode Thickness , Ionomer-to-Carbon Ratio , Ionomer Equivalent Weight , and Carbon Support. *J. Electrochem. Soc.* **158**, 467–475 (2011).
23. Spry, D. B., Goun, A., Glusac, K., Moilanen, D. E. & Fayer, M. D. Proton Transport and the Water Environment in Nafion Fuel Cell Membranes and AOT Reverse Micelles. *J. Am. Chem. Soc.* **129**, 8122–8130 (2007).
24. Antolini, E. Environmental Carbon supports for low-temperature fuel cell catalysts. *Applied Catalysis B: Environmental* **88**, 1–24 (2009).
25. Makharia, R, Mathias, M.F., & Baker, D.R. Measurement of Catalyst Layer Resistance in PEFCs Using Electrochemical Impedance Spectroscopy. *J. Electrochem. Soc.* **152**, A970–A977 (2009).
26. Wan, X., Liu, X., Li, Y., Yu, R., Zheng, L., Yan, W., Wang, H., Shui, J., Fe–N–C electrocatalyst with dense active sites and efficient mass transport for high-performance proton exchange membrane fuel cells. *Nature Catalysis* **2**, 259-268 (2019).
27. Myers, D., and Zelenay, P. ElectroCat presentation, U.S. DOE 2018 Hydrogen and Fuel Cell Program AMR Proceedings; 2018, [https://www.hydrogen.energy.gov/pdfs/review18/fc160\\_myers\\_2018\\_o.pdf](https://www.hydrogen.energy.gov/pdfs/review18/fc160_myers_2018_o.pdf)

28. Ahluwalia, R. K., Wang, X. & Steinbach, A. J. Performance of advanced automotive fuel cell systems with heat rejection constraint. *J. Power Sources* **309**, 178–191 (2016).
29. Zelenay, P. and Myers, D. ElectroCat presentation, U.S. DOE 2019 Hydrogen and Fuel Cell Program AMR Proceedings; 2019, [https://www.hydrogen.energy.gov/pdfs/review19/fc160\\_myers\\_zelenay\\_2019\\_o.pdf](https://www.hydrogen.energy.gov/pdfs/review19/fc160_myers_zelenay_2019_o.pdf)
30. Chen, M., He, Y., Spendelow, J.S., Wu, G., Atomically Dispersed Metal Catalysts for Oxygen Reduction, *ACS Energy Letters*, In press, (2019).
31. Shao, Y. Dodelet, J.-P., Wu, G., Zelenay, P. PGM-Free Cathode Catalysts for PEM Fuel Cells: A Mini-Review on Stability Challenges, *Advanced Materials*, 1807615, (2019).

## Table of Contents Graphic

### High Fuel Cell Power Density with Platinum-free Cathodes



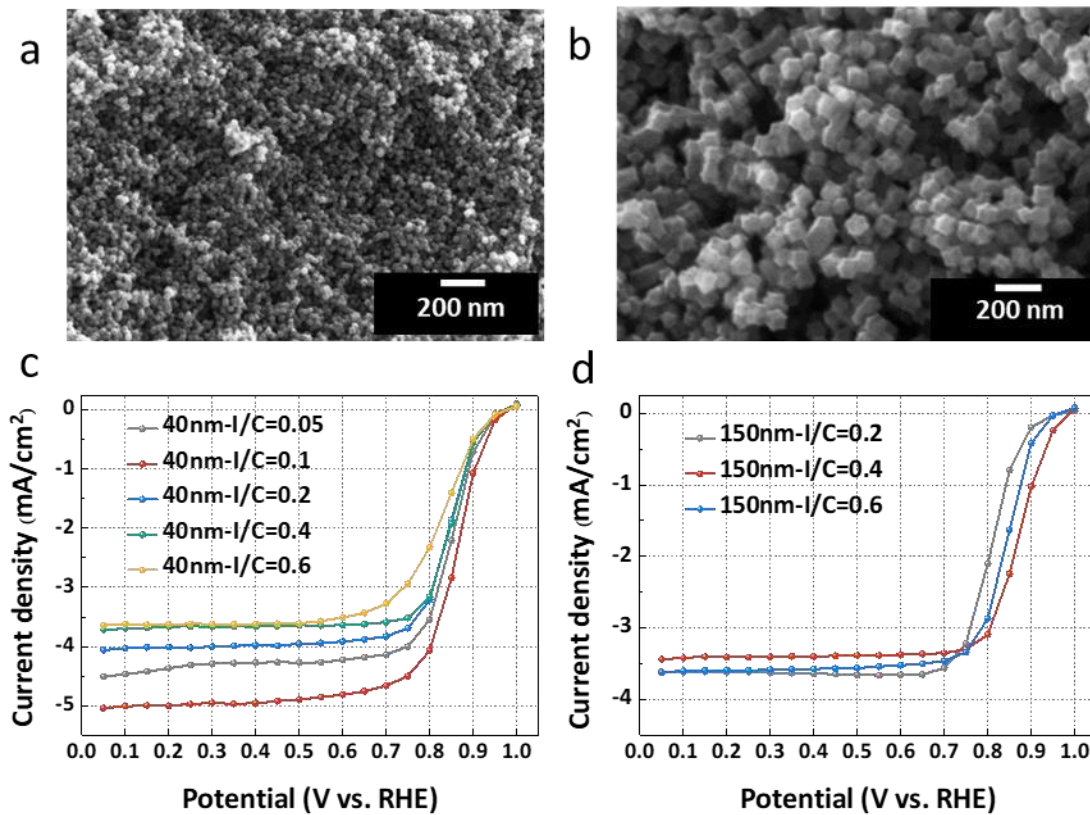


**Fig. 1 | RDE Characterization of Fe-MOF catalysts.** SEM images of catalysts containing FeMOF catalysts with different nominal primary particle diameters: 40 nm (a) and 100 nm (b). RDE polarization curves for ORR for 40 nm (c) and 150 nm (d) primary particles for electrodes prepared for a range of I/C ratios.

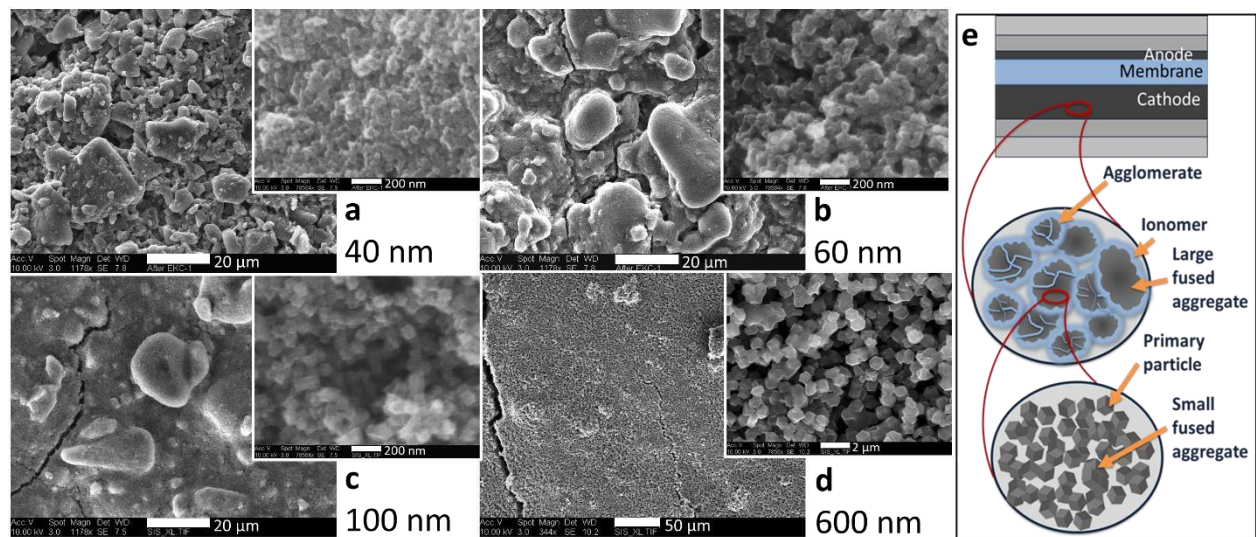


**Fig. 2 | Cathode catalyst layer structure. a-d**, SEM images of GDEs containing Fe-MOF catalysts with different primary particles: 40 nm (**a**), 60 nm (**b**), 100 nm (**c**), and 600 nm (**d**). **e**, Schematic representation of the cathode catalyst layer structure.

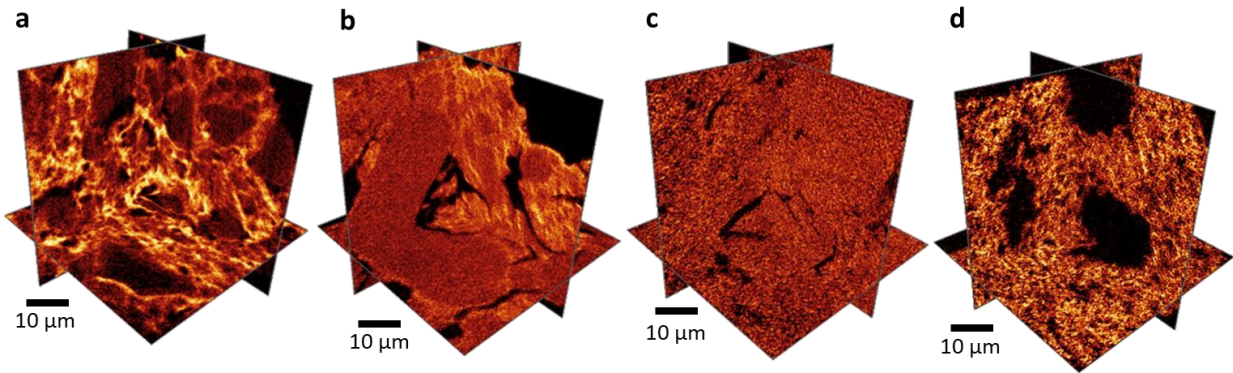


**Fig. 3 | Ionomer distribution in the cathode catalyst layer.** Nano-CT imaging of the ionomer distribution in cathodes of Fe-MOF catalysts with different primary particles and I/C: 40 nm and I/C 1 (**a**), 60 nm and I/C 0.6 (**b**), 100 nm and I/C 0.6 (**c**), and 600 nm and I/C 0.6 (**d**).

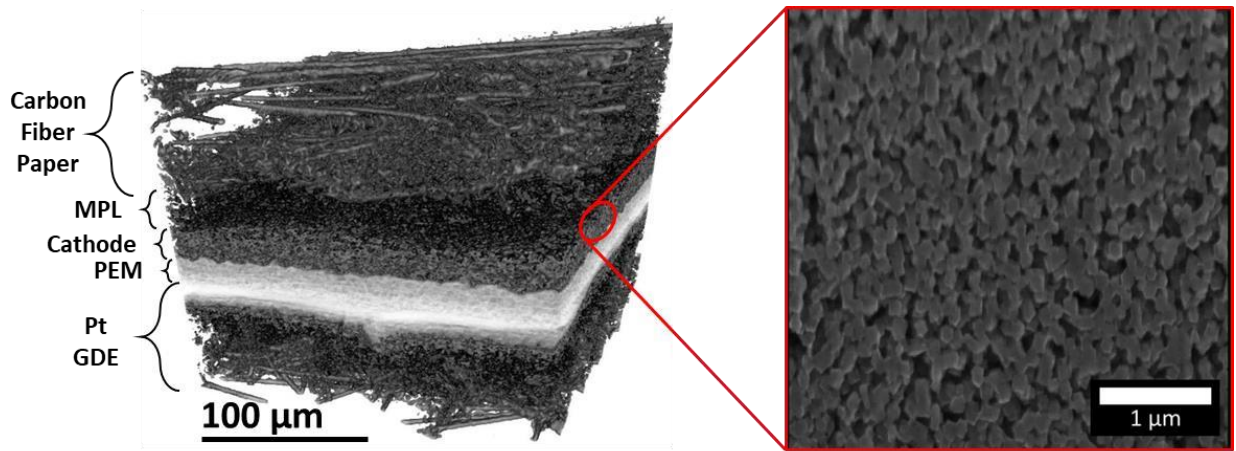


**Fig. 4 | Internal structure of the cathode and MEA.** Micro-CT imaging of the assembled MEA and cross-section of the cathode imaged using PFIB-SEM with 2 nm pixels. The cathode was prepared using 100 nm size catalyst with an I/C of 0.6.

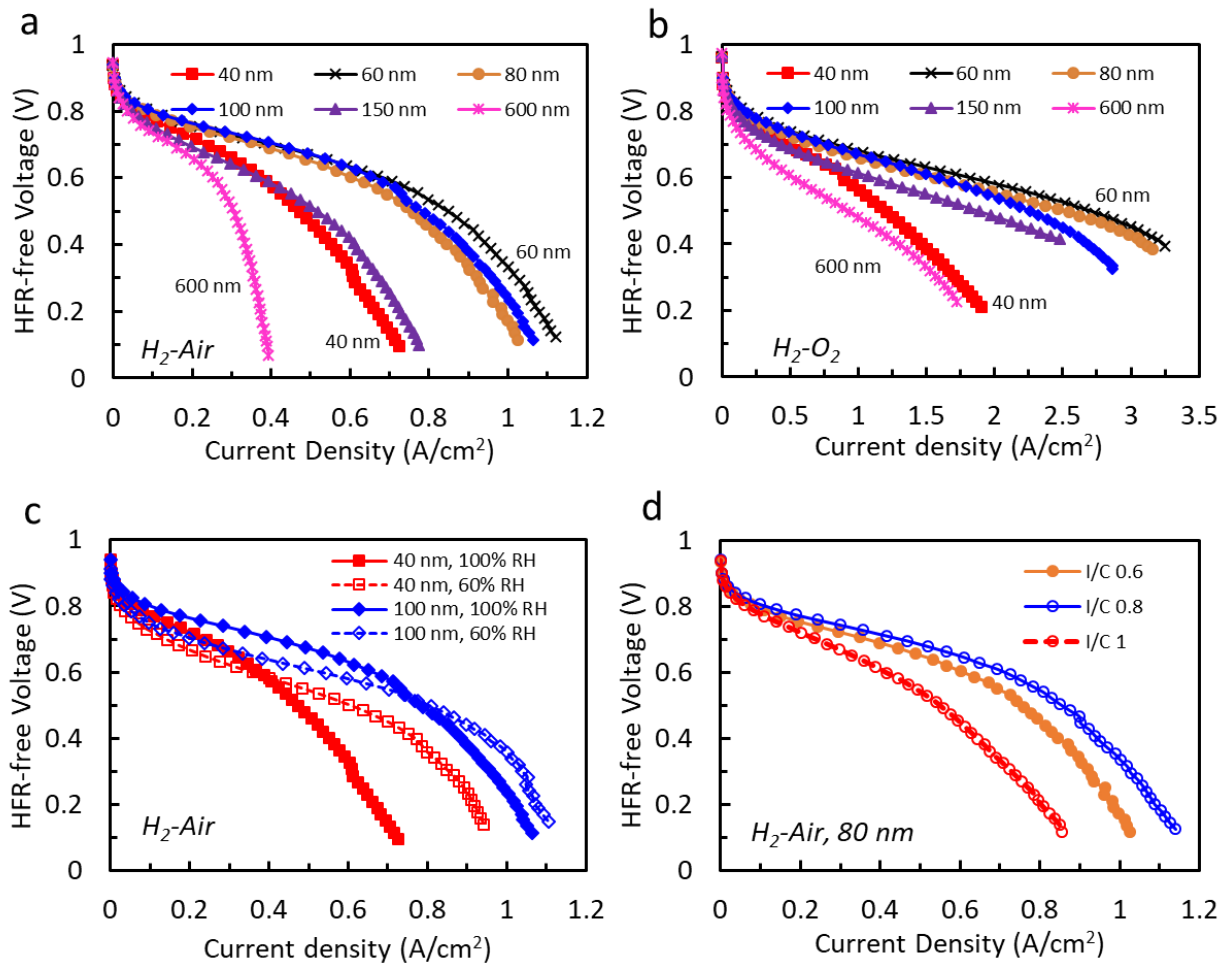


**Fig. 5 | Fuel cell performance of Fe-MOF catalysts with different primary particles. a,b,** Polarization curves obtained under air (a) and O<sub>2</sub> (b) for MEAs with cathodes prepared from FeMOF catalysts with different primary particles at 100% RH with I/C of 0.6. c, Polarization curves obtained under air for MEAs with cathodes prepared from the 40 nm and 100 nm size catalyst at 60% RH and 100% RH. d, Polarization curves obtained under air for MEAs prepared from the 80 nm size catalyst with various I/C at 100% RH. Conditions: 4 mg/cm<sup>2</sup> cathode loading, Nafion 212 membrane, cell temperature: 80°C; flow rate H<sub>2</sub>/Air: 200/200 sccm, 1 atm H<sub>2</sub>/Air partial pressure.

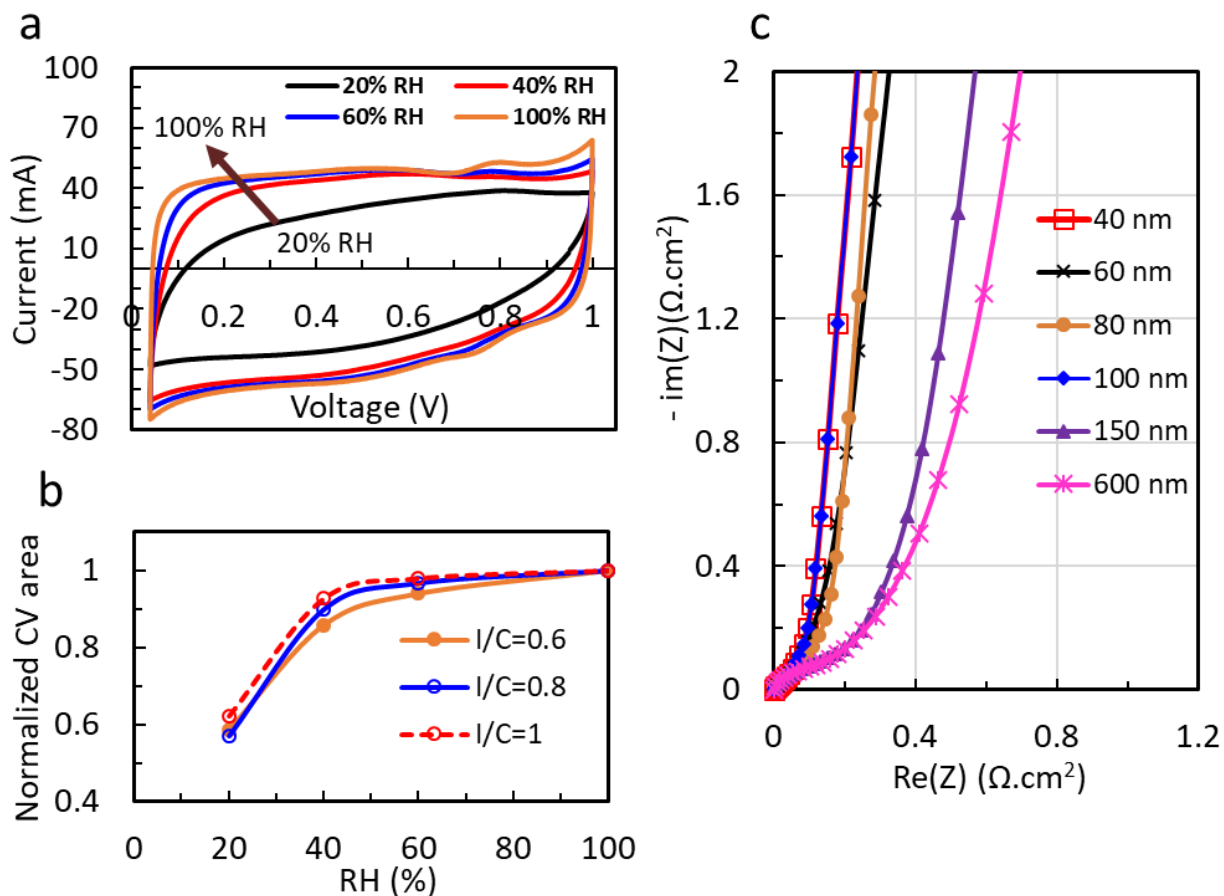


**Fig. 6 | Surface area and proton resistance. a,** CVs of an MEA prepared from the 80 nm size catalyst with I/C 0.6 at various RH. **b,** Variation in CV area of MEAs prepared from the 80 nm size catalyst with various I/C. **c,** Nyquist plots of impedance spectra with HFR subtracted as obtained under  $H_2/N_2$  at 0.5 V for MEAs prepared from catalysts with different primary particles with an I/C of 0.6.

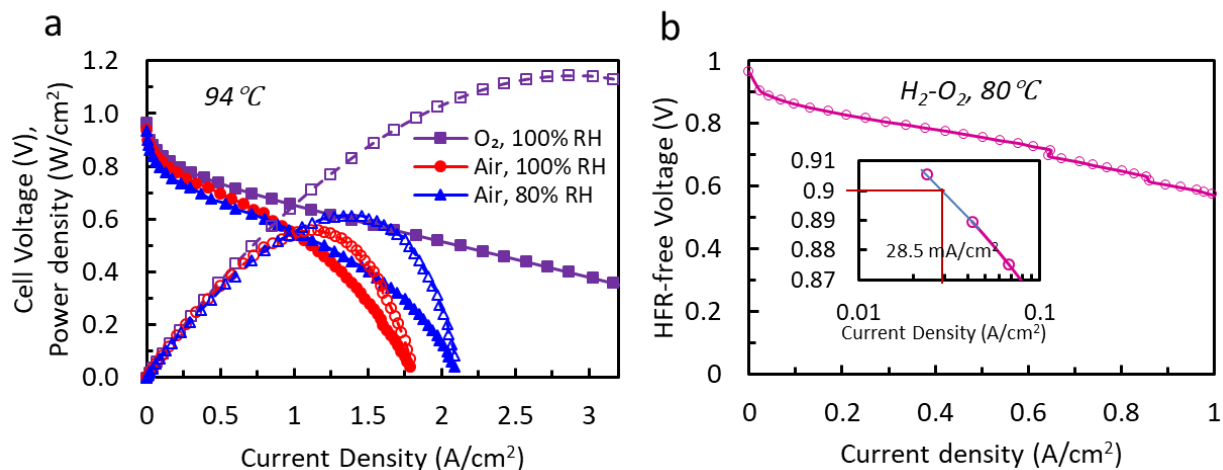


**Fig. 7 | High MEA Performance.** **a**, Polarization and power density curves obtained under air and O<sub>2</sub> for MEAs prepared from the 100 nm size catalyst. Conditions: 4.0 mg/cm<sup>2</sup> loading, I/C of 0.6, Nafion 211 membrane, cell temperature: 94°C; flow rate H<sub>2</sub>/air or O<sub>2</sub>: 200/1000 sccm, 1.7 atm H<sub>2</sub>/air or O<sub>2</sub> partial pressure. **b**, Polarization curve obtained under O<sub>2</sub> for an MEA prepared from the 100 nm size catalyst. Conditions: 6 mg/cm<sup>2</sup> loading, I/C of 1, Nafion 117 membrane, cell temperature: 80°C; flow rate H<sub>2</sub>/O<sub>2</sub>: 200/200 sccm, RH: 100%, 1 atm H<sub>2</sub>/O<sub>2</sub> partial pressure.

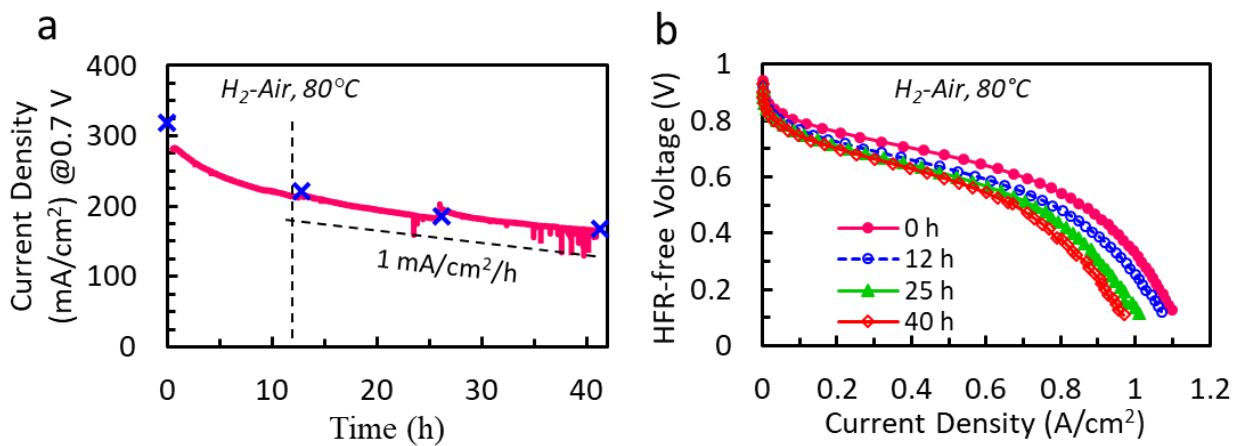


**Fig. 8 | Stability of Fe-MOF catalyst in an MEA. a,** Stability of the 100 nm size catalyst during a potentiostatic experiment at 0.7 V. **b,** Polarization curves obtained under air intermittently during the stability test. Conditions: catalyst loading: 4.0 mg/cm<sup>2</sup>, cell temperature: 80°C; flow rate H<sub>2</sub>/air: 200/200 sccm, RH: 100%, 1 atm H<sub>2</sub>/air partial pressure and Nafion 212 membrane.